Theor Chem Acc (2003) 110: 196–204
DOI 10.1007/s00214-003-0472-0

Theoretical
Chemistry Accounts

Regular article

The migratory insertion of carbon monoxide and methyl isocyanide into zirconium–carbon and titanium–carbon bonds anchored to a calix[4]arene moiety: a dynamical density functional study

Filippo De Angelis[1], **Simona Fantacci**[1], **Antonio Sgamellotti**[1], **Nazzareno Re**[2]

[1]Istituto CNR di Scienze e Tecnologie Molecolari (ISTM), c/o Dipartimento di Chimica,Università di Perugia, 06123 Perugia, Italy
[2]Facoltà di Farmacia,Università G. D'Annunzio, 66100Chieti, Italy

Received: 31 March 2002 / Accepted: 19 October 2002 / Published online: 16 September 2003

Abstract. The energetics and reaction mechanism of the migratory insertion of carbon monoxide and methyl isocyanide into the zirconium–carbon and titanium–carbon bonds in [calix[4](OMe)$_2$(O)$_2$–*M*–Me$_2$], (*M* = Zr, Ti), have been investigated by combining static and dynamic density functional calculations. Two steps have been characterized: the coordination of the incoming nucleophilic moiety leading to relatively stable facial adducts; its subsequent insertion into the *M*–C bond, leading to η^2-bound acyl or iminoacyl complexes, providing a rationale for the different behavior of CO and MeNC towards both insertion and deinsertion reactions. Our results indicate that the rate-determining step for the overall MeNC insertion into the *M*–C bond is its coordination to the electron-deficient metal center, with the titanium system featuring a higher energy barrier (12.7 versus 5.5 kcal mol^{-1}). Ab initio molecular dynamics simulations have been performed on the Zr system by means of the Car–Parrinello method, to study the hitherto inaccessible mechanistic features of the insertion reactions.

Keywords: Migratory insertion – Calix[4]arene moiety – Dynamical density functional calculations

1 Introduction

Tracing the reaction mechanism of complex organometallic reactions represents a challenging field in theoretical and computational chemistry, owing to the intrinsic complexity of the potential-energy surface involved in the reactive process. Indeed, the presence of a metal center showing different oxidation states and coordination modes coupled to the usually large size of the reactive system results in a large number of local minima connected by several transition states, which can be hardly sampled by "static" methods, based on local geometry optimization techniques. A powerful tool, which has become widely applied to problems of chemical interest, is represented by ab initio molecular dynamics (AIMD) based on the Car–Parrinello method [1]. Such an approach allows the dynamical sampling of the potential-energy surface at finite temperature, providing useful insights into the reaction mechanism and evidencing the presence of possible reaction intermediates. In the following, we exploit such methodology combining static density functional theory (DFT) calculations with Car–Parrinello AIMD simulations to study the migratory insertion reaction of carbon monoxide and isocyanides into zirconium–carbon bonds anchored to a calix[4]arene moiety; this combined strategy has already been successfully applied to the study of similar CO insertions [2,3].

The migratory insertion of CO and isocyanides into metal–alkyl bonds has been observed for most of the early *d*-block metals and has received much attention from synthetic, mechanistic and theoretical points of view [4,5,6,7,8,9,10]. Spectroscopic data and structural studies have indicated that all isolable CO insertion products contain η^2-acyl groups, where both carbon and oxygen atoms are bound to the metal center, as opposed to an η^1 coordination in which only the carbon is bound to the metal center (Scheme 1). In recent years the insertion of isocyanides into early transition

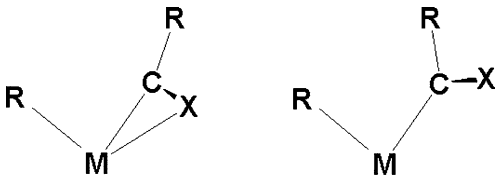

η^2-coordination η^1-coordination

Contribution to the Björn Roos Honorary Issue

Correspondence to: A. Sgamellotti
e-mail: sgam@thch.unipg.it

metal–alkyl bonds has been extensively studied because the resulting η^2-iminoacyls are much more accessible and less reactive than the corresponding η^2-acyl derivatives. Analogously to η^2-acyl complexes, η^2-iminoacyls undergo insertion of a further alkyl group into the iminoacyl moiety, to generate an η^2-imine, or the uptake of a second isocyanide molecule to give an enediamide [11,12,13]. However, unlike CO, isocyanides hardly undergo deinsertion but rather may easily give rise to multiple insertion into various metal–carbon bonds, providing useful synthetic routes to nitrogen-containing organic compounds [11].

In particular, the multistep migratory insertion of CO and isocyanides into the metal–carbon bonds of the ZrR_2 fragment anchored to a the dimethoxycalix[4]arene dianion [*p*-Bu^t-calix[4](OMe)$_2$(O)$_2$]$^{2-}$ has been reported recently [14]. While the reaction of [*p*-Bu^t-calix[4](OMe)$_2$(O)$_2$ZrMe$_2$], **1**, with CO proceeds via a two-step migration to give directly the corresponding η^2-acetone regardless of the experimental conditions [14], the analogous reaction of **1** with Bu^{t}NC leads to an η^2-imine species only at room temperature; at low temperature the same process shows the preferential migration of the second alkyl group to an incoming Bu^{t}NC, to give a bis-η^2-iminoacyl complex [14].

A general study on the temperature selectivity of the overall reaction for the Zr system has recently been performed by us [15]; in the present case we investigate in detail the isocyanide coordination to the [*p*-Bu^t-calix[4](OMe)$_2$(O)$_2$ZrMe$_2$] moiety, and compare results for CO and MeNC insertions into the Zr–C bond in the same complex [2,15]. Moreover, since experimental data are not available for the reactivity of the corresponding Ti fragment, we characterized the stationary points of the potential-energy surface for the migratory insertion of MeNC into the titanium–carbon bond in the analogous [*p*-Bu^t-calix[4](OMe)$_2$(O)$_2$TiMe$_2$] system.

Geometry optimizations were performed for all the minima involved in the coordination and insertion reactions leading to the η^2-iminoacyl species, linear transit (LT) scans of the potential-energy surfaces were performed to estimate the energy barriers and transition-state structures were located starting from the maximum-energy structures obtained from the LT curves. Car–Parrinello simulations were employed to study the detailed dynamical features of CO and MeNC migratory insertion reactions from the corresponding [*p*-Bu^t-calix[4]-(OMe)$_2$(O)$_2$ZrMe$_2$]–(CO or MeNC) adducts.

2 Computational details

2.1 Static DFT calculations

We model the [*p*-Bu^t-calix[4](OMe)$_2$(O)$_2$] ligand by replacing the Bu^t para substituents by H atoms; it has been shown that for this class of compounds this approximation does not affect the electronic properties of the systems investigated [16]. Also, the Bu^t-NC group was modeled by MeNC.

All the static DFT calculations reported in this paper are based on the Amsterdam density functional (ADF) program package described elsewhere [17,18,19]. Its main characteristics are the use of a density-fitting procedure to obtain accurate Coulomb and exchange potentials in each self-consistent-field cycle, the accurate and efficient numerical integration of the effective one-electron Hamiltonian matrix elements and the possibility to freeze core orbitals. The molecular orbitals were expanded in an uncontracted double-zeta (DZ) Slater-type orbital (STO) basis set for all atoms with the exception of the transition-metal orbitals for which we used a DZ STO basis set for n*s* and n*p* and a triple-zeta STO basis set for n*d* and (n + 1)*s* [20]. As polarization functions, one 5*p*, one 4*p*, one 3*d* and one 2*p* STO were used for Zr, Ti, O, N and C, and H respectively; the frozen cores were 1*s*-4*p* for Zr and 1*s* for C and O. Geometry optimizations were performed without any symmetry constraints, using the Vosko–Wilk–Nusair local density approximation (LDA) parameterization [21] and including the Becke [22] and Perdew–Wang [23] gradient corrections to the exchange and correlation, respectively. The energy profiles for the first MeNC coordination and insertion processes, as well as those for the second MeNC insertion and coordination, were traced by means of LT calculations; transition states were located using the Powell method [24] implemented in the ADF package.

2.2 Car-Parrinello calculations

Molecular dynamics simulations were carried out with the Car–Parrinello (CP) method [25,26]. For the LDA exchange–correlation functional the Perdew–Zunger parameterization [27] was used, while the gradient–corrected functional was taken from Ref. [28]. Core states are projected out using pseudopotentials. For Zr, C, O, N and H "ultrasoft" pseudopotentials were generated according to the scheme proposed by Vanderbilt [26]. The wavefunctions were expanded in plane waves up to an energy cutoff of 25 Ry. Periodic boundary conditions were used by placing the model molecule in a cubic box of 15.87 Å, keeping a minimum of 5.0 Å between repeated images, sufficiently large to avoid any coupling between periodic images. The equations of motion were integrated using a time step

Table 1. Optimized geometrical parameters (angstroms and degrees) of [calix[4]O$_2$(OMe)$_2$]Zr(CH$_3$)$_2$, **1**, using the Amsterdam density functional (*ADF*) and Car–Parrinello (*CP*) programs, compared with X-ray data observed for the dimethyl Zr complex [14], and of the [calix[4]O$_2$(OMe)$_2$]Ti(CH$_3$)$_2$ complex, **1′**, using the ADF program

Parameters	**1**, *M* = Zr			**1′**, *M* = Ti
	Exp. [14]	CP	ADF	ADF
$R_{M-O_{1,3}}$	1.960	2.020	2.060	1.894
$R_{M-O_{2,4}}$	2.298	2.366	2.389	2.307
$R_{M-C_{\alpha,\beta}}$	2.332	2.323	2.336	2.176
$\angle O_1 - M - O_3$	102.4	104.3	104.7	104.8
$\angle O_2 - M - O_4$	153.9	154.7	154.5	161.1
$\angle M - O_1C_1$	175.9	174.1	174.3	171.2
$\angle M - O_2C_2$	118.2	113.4	113.3	112.0
$\angle C_\alpha - M - C_\beta$	83.7	79.4	79.1	78.8

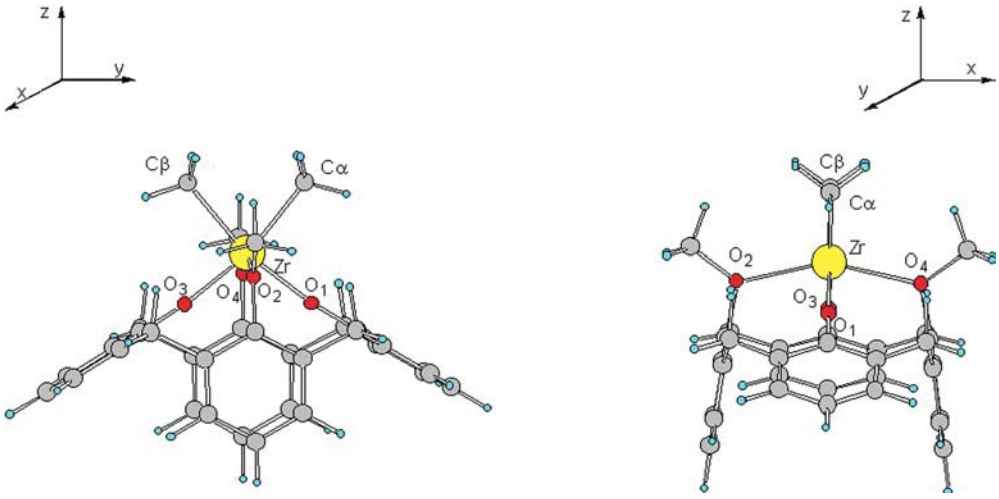

Fig. 1. Optimized structure of [calix[4](OMe)$_2$(O)$_2$Zr(Me)$_2$] complex, **1**

of 10 au (0.242 fs) with an electronic fictitious mass μ = 1000 au.

To check the consistency of the CP and ADF programs we compare the geometries of the model [calix[4](OMe)$_2$(O)$_2$Zr(Me)$_2$] complex **1**, optimized at both levels of theory with that of [*p*-Bu^t-calix[4](OMe)$_2$(O)$_2$-Zr(CH$_2$Ph)$_2$], the closest experimental compound for which X-ray data are available [14]. Good agreement between the two approaches and experimental data is shown in Table 1, suggesting that metal–ligand interactions are accounted for with the same accuracy within both approaches.

3 Results and discussion

3.1 Structural and electronic properties of [calix[4](OMe)$_2$(O)$_2$Zr(Me)$_2$]

The geometry of complex **1** was optimized under C_{2v} symmetry constraints [2], with the two methyl carbon atoms bound to zirconium lying in the *yz* plane (Fig. 1). Hereafter we refer to C_α and C_β as, respectively, the carbon of the methyl group undergoing the MeNC insertion and the remaining methyl carbon, O_1 and O_3 as the phenoxo oxygens and O_2 and O_4 as the methoxy oxygens.

Frontier orbital analysis performed on complex **1** [2] revealed an isolated lowest unoccupied molecular orbital (LUMO) of essentially zirconium d_{xz} character (Fig. 2), which represents the only vacant molecular orbital to which the incoming nucleophilic ligand (CO or MeNC) can donate prior to insertion. The [calix[4](OMe)$_2$(O)$_2$Zr]$^{2+}$ metal fragment shows four noncoplanar low-lying vacant metal orbitals, $1a_1(d_{z^2})$, $1b_1(d_{xz})$, $1b_2(d_{yz})$ and $1a_2(d_{xy})$ [14]; such a spatial orientation of these orbitals has been related to a facial arrangement of the three additional ligands (*L*) in a [calix[4](OMe)$_2$(O)$_2$Zr*L*$_3$] species, and was quantified by the higher stability of the facial adduct which is the only stable adduct in the CO coordination process [2]. However, the presence of a Bu^t bulky substituent on the isocyanide group in the experimental complex can partially affect the topology of the isocyanide approach with respect to CO.

3.2 CO and MeNC coordination to [calix[4](OMe)$_2$(O)$_2$Zr(Me)$_2$]

The isocyanide migratory insertion is supposed to be initialized by the coordination of the nucleophilic MeNC group to the electron-deficient zirconium center of [*p*-Bu^{t}calix[4](OMe)$_2$(O)$_2$Zr(Me)$_2$]. Owing to the peculiar electronic structure of complex **1** and the spatial extension of the LUMO, we expect that the most favorable approach of MeNC occurs along a line in the plane bisecting the Me–Zr–Me angle (*xz*) forming an angle of about 45° with the *z*-axis, leading to a facial adduct, as found for the CO coordination in Ref. [2].

To check this point we optimized the geometry of the [calix[4](OMe)$_2$(O)$_2$Zr]-(MeNC) adduct without any symmetry constraints and also with two possible meridional geometries of C_s symmetry (one with the

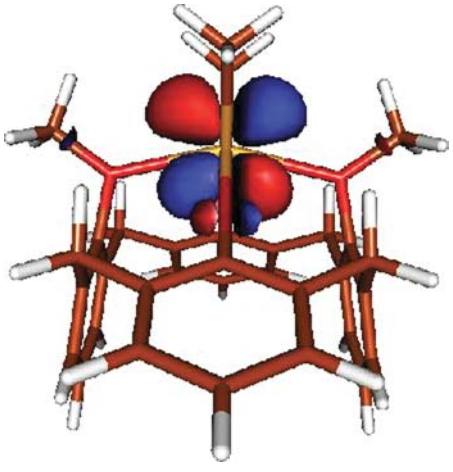

Fig. 2. Isodensity surface plot (0.04 contour value) of the lowest unoccupied molecular orbital orbital of [calix[4](OMe)$_2$(O)$_2$ Zr(Me)$_2$]

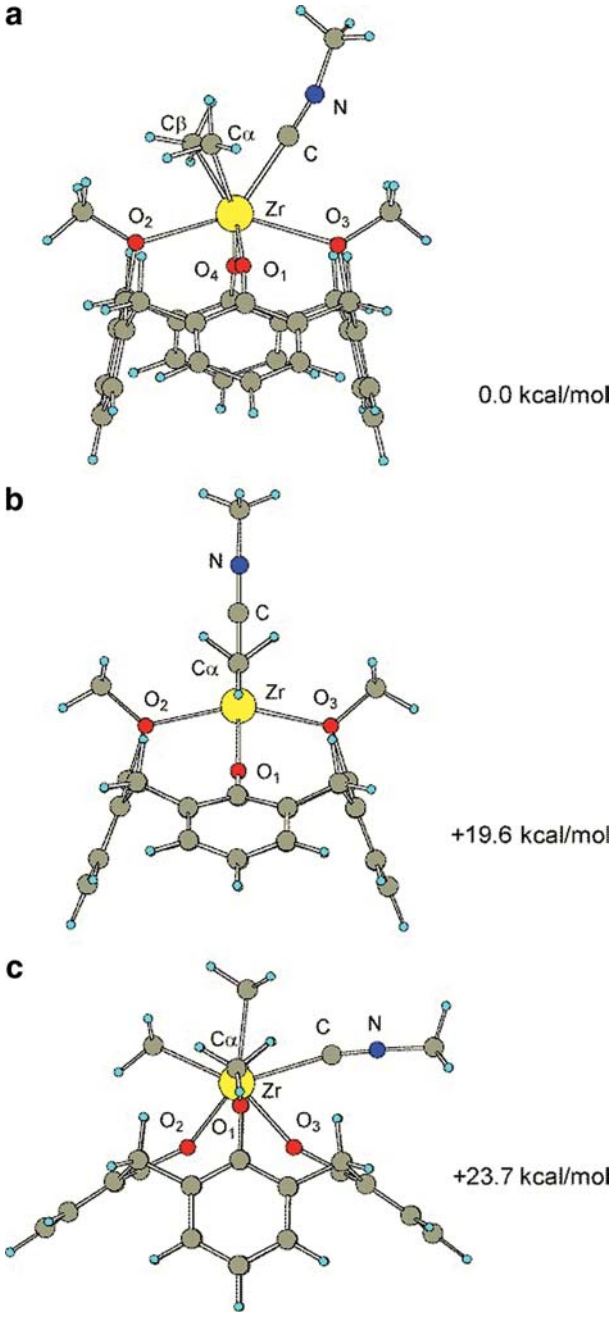

Fig. 3. Optimized structures of the [calix[4](OMe)$_2$(O)$_2$ZrMeNC] adducts, **2a**, **2b** and **2c**

MeNC ligand lying between the two CH_3 groups and one with the MeNC ligand placed on the side of one methyl group, (Fig. 3). The facial geometry **2a** was found to be the lowest in energy (9.4 kcal mol^{-1} below the starting reagents, 5.0 when accounting for basis set superposition error, BSSE, correction); this value is 2.7 kcal mol^{-1} smaller than that found for the corresponding CO adduct, see later. The "central", **2b**, and "lateral", **2c**, meridional isomers were found 19.6 and 23.7 kcal mol^{-1} above **2a**, respectively; therefore they are not stable with respect to the free reagents (dimethyl complex **1** + MeNC). Notably, this is the same trend already observed for CO coordination to **1**, showing that only a facial approach leads to stable adducts, consistent with the frontier orbital picture presented earlier.

The optimized geometry of **2a** (Table 2) reflects the geometrical perturbation due to the coordination of MeNC which prepares the insertion reaction. The Zr–$C_{\alpha,\beta}$ bond lengths are about 0.5–0.7 Å longer than in the dimethyl complex **1**, while the Zr–O_{2-4} distances were found to be 0.1–0.2 Å longer. The long Zr–C(CNMe) distance, 2.273 Å, reflects the weak interaction between the MeNC ligand and the [calix[4](OMe)$_2$(O)$_2$ZrMe$_2$] fragment, as expected since the MeNC ligand cannot exploit any stabilizing π back-donation interaction with a d^0 electron-deficient metal center such as Zr(IV).

With the aim of evaluating the energy barrier for MeNC coordination, we performed a LT scan of the potential-energy surface of the [calix[4](OMe)$_2$(O)$_2$Zr] + MeNC system, assuming the Zr–CN distance as the reaction coordinate; geometry optimizations were performed by constraining the Zr–CN distance in the range 4.0–2.2 Å, the latter value being close to the equilibrium Zr–CN distance in complex **2a**, relaxing all the other geometrical parameters. The resulting energy profile is

Table 2. Optimized geometrical parameters (bond lengths in angstroms and angles in degrees) of MeNC adducts, **2a** and **2a′**, η^1-acyl complexes, **3** and **3a′**, and η^2-acyl complexes, **4** and **4′**

Parameters	M = Zr			M = Ti		
	2a	**3**	**4**	**2a′**	**3′**	**4′**
R_{M-O_1}	2.063	2.027	2.066	1.909	1.877	1.918
R_{M-O_2}	2.484	2.399	2.433	2.410	2.302	2.342
R_{M-O_3}	2.057	2.015	2.052	1.904	1.875	1.915
R_{M-O_4}	2.574	2.504	2.430	2.675	2.574	2.391
R_{M-C_α}	2.402	3.070	–	2.296	3.021	–
R_{M-C_β}	2.389	2.310	2.342	2.288	2.176	2.199
R_{M-CN}	2.270	2.308	2.280	2.060	2.171	2.122
R_{M-N}	–	–	2.270	–	–	2.140
R_{C-N}	1.180	1.283	1.279	1.187	1.276	1.265
$R_{C_\alpha-CN}$	2.510	2.537	1.496	2.307	1.530	1.512
$\angle O_1MO_3$	106.2	120.7	103.3	108.2	120.0	102.5
$\angle O_2MO_4$	147.6	154.0	150.0	152.4	157.5	155.0
$\angle MCN$	177.5	132.5	73.2	179.2	128.0	73.5

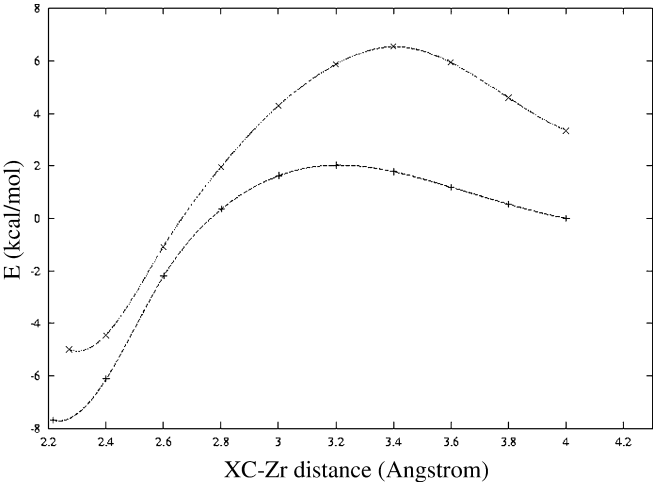

Fig. 4. Potential-energy profiles for the coordination of CO (*lower curve*) and Me–NC (*upper curve*)

compared with that of CO coordination in Fig. 4; the two curves have been rescaled in such a way that the zero of the energies corresponds to the BSSE-corrected energy of the free reagents (**1** + CO or MeNC). It is interesting to notice that the estimated barrier for MeNC coordination is sensitively higher than that computed for CO, 6.4 versus 2.0 kcal mol^{-1}, with a longer-ranged interaction, probably reflecting the larger steric hindrance of the isocyanide species. In particular, in the MeNC case starting from the structure of the maximum of the curve, we located the transition state, $\mathbf{TS}_{1\rightarrow 2a}$, finding an energy barrier of 5.5 kcal mol^{-1}.

To disentangle electronic and steric effects, we investigate in detail the electronic structure of both CO and MeNC ligands. The energies and composition in terms of atomic contributions of frontier orbitals of the two ligands are reported in Table 3. The highest occupied molecular orbital (HOMO) of MeNC, the $6a'$ orbital, lying at en energy of -7.39 eV, is an *sp*-hybridized lone pair entirely localized at the isocyanide carbon, with the LUMOs, $7a'$ and $3a''$, lying at about -0.64 eV, of π^* character. Such a frontier orbital picture reflects the σ-donor and π-acceptor properties of the MeNC ligand, depending on the electronic properties of the interacting transition metal. The electronic structure of CO is qualitatively similar to that of MeNC, with the carbon lone pair, the 3σ orbital, lying at -9.40 eV (Table 3). Therefore, although the higher HOMO energy would favor the MeNC coordination, its higher steric hindrance probably leads to a higher energy barrier for MeNC coordination compared to CO, a factor that should also be responsible for the slight destabilization of the MeNC adduct **2a** with respect to the corresponding CO adduct.

3.3 CO and MeNC insertion into the Zr–C bond and formation of the η^2-iminoacyl complex

3.3.1 Dynamics simulations

To understand the mechanism of the MeNC migratory insertion in the [*p*-Bu^t-calix[4](OMe)$_2$(O)$_2$ZrMe$_2$]-(MeNC) adduct, we carried out dynamics simulations on complex **2a**. We started the dynamics simulation by heating up the structure of the MeNC adduct **2a** in the DFT optimized geometry, to a temperature of 300° K. To obtain a thermal distribution of vibrational modes, the temperature was gradually increased (via rescaling of ionic velocities) in small steps. We did not apply any constraints to the molecular motion, allowing all the degrees of freedom to evolve naturally in time. The total time span of the simulation was 2.5 ps. The MeNC migratory insertion can be followed by studying the time evolution of the C_α–C(NMe), Zr–C_α(Me) and Zr–N distances. Indeed, the C_α–C distance is expected to be longer than 2.5 Å in reagent **2a**, where the two carbon atoms belong to two different ligands, while it is only about 1.5 Å in the iminoacyl product, where they are directly bound; the Zr–C_α distance is about 2.4 Å in **2a** and is expected to be much larger in the product where the methyl is no longer bound to the Zr center; the Zr–N distance is about 3.5 Å in **2a** and is expected to be smaller in the iminoacyl product.

The variation of the C_α–C and Zr–C_α distances is displayed in Fig. 5 as a function of the simulation time and clearly shows that the reactive MeNC migration takes place within about 0.6 ps, as testified by the fast decrease in the C_α–C distance from about 2.7 to about 1.5 Å. Thereafter, the C_α–C distance varies within the normal limits of a carbon–carbon vibration. At the same time the Zr–C_α distance follows an almost complementary trajectory with respect to the C_α–C distance and increases from about 2.4 up to about 3.7 Å, reflecting the methyl detachment from the metal center upon MeNC insertion. However, this parameter shows higher oscillations after 0.7 ps, since, at the end of the reaction, the Zr and CH_3 groups are no longer bound.

The time evolution of the Zr–N and C_α–C distances in MeNC insertion is displayed in Fig. 6a, while the time evolution of the Zr–O and C_α–C distances in CO insertion is displayed in Fig. 6b [2]. As can be noticed, the Zr–N distance is found to decrease from its initial value, about 3.5 Å, to about 2.2 Å, corresponding to a Zr–N bond in an η^2-iminoacyl species, **4**, within 0.9 ps. It is worth noting that the formation of the Zr–N bond is delayed by about 0.3 ps with respect to the C_α–C bond formation, suggesting the initial formation, after 0.6 ps, of a transient η^1-iminoacyl species, **3**, with a formed C_α–C bond and still a long Zr–N bond. Interestingly, formation of a transient η^1-bound isomer was observed also in the CO insertion reaction, (Fig. 6b), which subse-

Table 3. Frontier molecular orbitals (*MO*) of CO and MeNC molecules

MO	Occ.	*E*(eV)	Composition
MeNC			
$3a''$	0	−0.638	$65\%(p_x)_C, 24\%(p_x)_N$
$7a'$	0	−0.640	$18\%(p_z)_C, 48\%(p_y)_C, 16\%(p_y)_N$
$6a'$	2	−7.394	$61\%(s)_C, 25\%(p_z)_C, 9\%(p_y)_C$
$5a'$	2	−8.553	$8\%(p_z)_C, 20\%(p_y)_C, 14\%(p_z)_N, 36\%(p_y)_N$
$2a''$	2	−8.556	$32\%(p_x)_C, 50\%(p_x)_N$
CO			
2π	0	−2.250	$75\%(p_x)_C, 25\%(p_x)_O$ $75\%(p_y)_C, 25\%(p_y)_O$
3σ	2	−9.395	$60\%(s)_C, 30\%(p_z)_C, 9\%(p_z)_O$
1π	4	−12.026	$24\%(p_x)_C, 74\%(p_x)_O$ $24\%(p_y)_C, 74\%(p_y)_O$

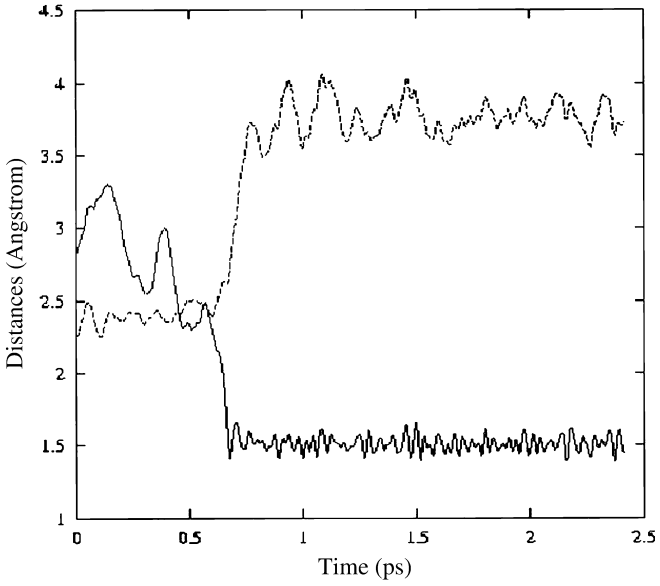

Fig. 5. Time evolution of C_α–C (*solid line*) and Zr-C_α (*dashed line*) distances in MeNC insertion

quently evolved to the corresponding η^2-acyl [2]. The short time stability of the η^1 isomer of both acyl and iminoacyl species (about 0.6 and about 0.3 ps, respectively) suggests a negligible barrier for the conversion of the η^1 into the η^2 isomers, the same result already found for CO insertion in bis(cyclopentadienyl) Zr dimethyl complexes [30].

To gain further insight into the mechanistic features of the migratory insertion reaction, we analyze the time evolution of the C–Zr–O_2–C_α and O_2–Zr–C_α–C_β dihedral angles in MeNC and CO insertions in Fig. 7a and b, respectively. Indeed, variation of the considered dihedral angles is determined by the relative motion of the methyl and carbonyl or isocyanide carbons (C_α and C, respectively). From Fig. 7a it appears that the MeNC migration is actually better described as an isocyanide insertion into the Zr–Me bond, as testified by the almost constant oscillations of the O_2–C_α–Zr–C_β dihedral angle around about 90° coupled to the fast decrease in the C–Zr–O_2–C_α dihedral angle from about 140 to about 100° within 0.9 ps, reflecting the isocyanide approach to the methyl prior to the C_α–C bond formation. On the other hand, from Fig. 7b it is clear how the reaction mechanism is reversed in CO insertion, with the inserting methyl attacking the resting carbonyl group, in agreement with the generally accepted mechanism of carbonyl migratory insertion reactions [29].

3.3.2 Static calculations

Dynamics simulations have shown that the final product of isocyanide insertion into the Zr–Me is the η^2-iminoacyl species **4**. We therefore optimized the geometry of the η^1- and η^2-iminoacyl species, **3** and **4**, without symmetry constraints, finding two structures with the CN group lying almost perpendicular to the *yz* plane, as shown in Fig. 8. The geometrical parameters of complexes **3** and **4** are reported in Table 2; it is worth

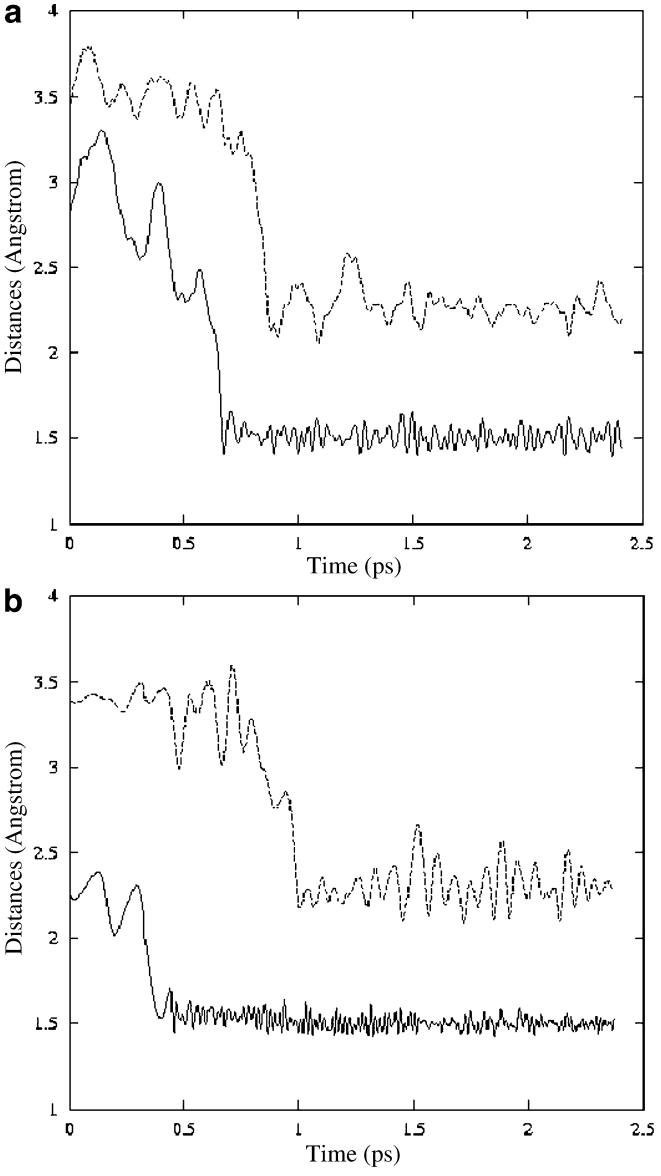

Fig. 6. Time evolution of **a** Zr–N (*dashed line*) and C_α–C (*solid line*) distances in MeNC insertion, and **b** Zr–O (*dashed line*) and C_α–C (*solid line*) distances in CO insertion

noting that the calixarene ligand is particularly flexible and rearranges on the basis of the two different coordination modes. Indeed, the O_1ZrO_3 and O_2ZrO_4 angles close in the η^2-iminoacyl complex by about 16° and about 5°, respectively, with respect to the corresponding values in the η^1 isomer. Both the η^1- and the η^2-bound iminoacyls are found to be much stable than the facial adduct **2a**, by 27.0 and 35.6 kcal mol^{-1}, respectively.

To provide an estimate of the energy barrier associated with the insertion reaction, we traced the energy profile for the formation of the η^1-iminoacyl species by means of a LT calculation, constraining the approximate reaction coordinate, the C(NMe)–C_α distance, to the range 2.5–1.5 Å and relaxing all the other geometrical parameters. The C(NMe)–C_α distance represents a natural choice for a reaction coordinate, since its variation corresponds to the formation of the iminoacyl C_α–C

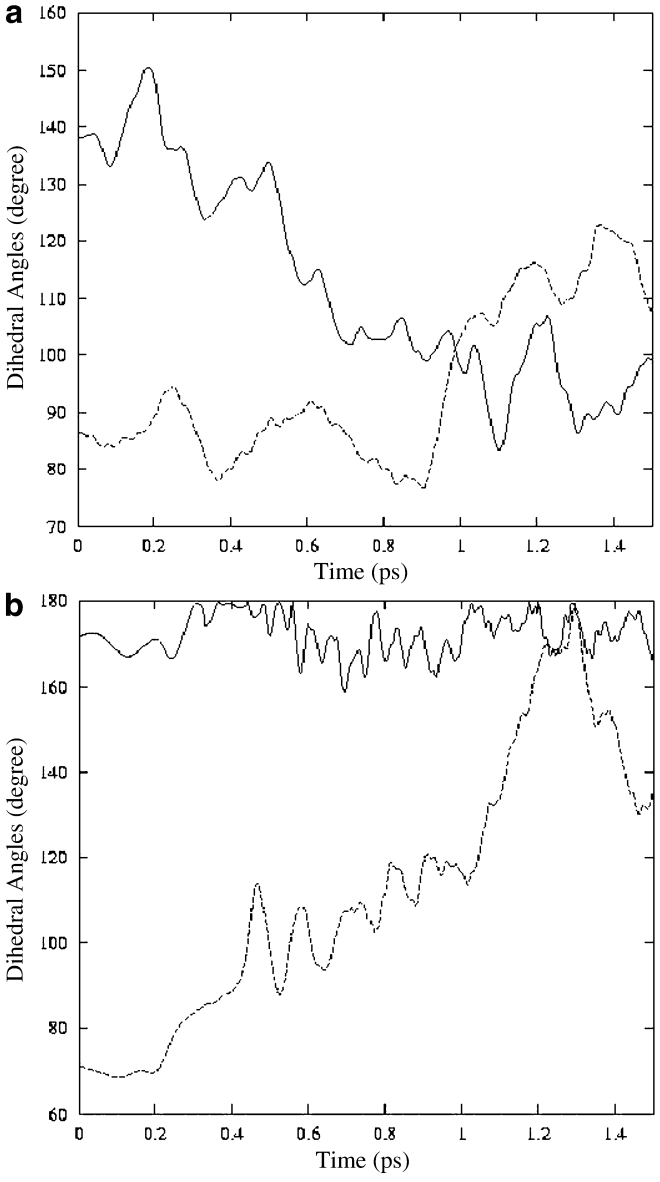

Fig. 7. Time evolution of the C_α–Zr–O_2–C_β and the C–Zr–O_4–C_β dihedral angles in **a** CO and **b** MeNC insertions

bond, as shown by the dynamics simulation. Starting from the maximum-energy LT structure, we optimized the geometry of the transition state for MeNC migratory insertion, $\mathbf{TS}_{2a\rightarrow3}$, finding it only 0.6 kcal mol^{-1} above **2a**. We therefore see how both MeNC and CO migratory insertions are kinetically favored processes, even though MeNC insertion is computed to be much more exothermic than the corresponding CO insertion (35.6 versus 19.4 kcal mol^{-1}); see Fig. 9 for a summary of the computed energetics.

3.4 MeNC coordination and insertion into the Ti–C bond

We optimized the geometry of the [calix[4](OMe)$_2$(O)$_2$ Ti(Me)$_2$] complex **1′** under C_{2v} symmetry constraints; the same orientation and atom labeling employed for the Zr complex **1** is maintained here, see earlier. The main optimized geometrical parameters are reported in Table 1; the optimized structure is qualitatively similar to that found for the [calix[4](OMe)$_2$(O)$_2$Zr(Me)$_2$] complex, showing a pseudo-octahedral coordination of the six ligands. The titanium–oxygen(carbon) bonds are computed to be shorter than the corresponding zirconium–oxygen(carbon) values in **1**, as expected on the basis of the smaller atomic radius of Ti compared to Zr. Consistently, we compute a O_2TiO_4 angle about 7° larger than the O_2ZrO_4 angle in **1**, reflecting the more effective octahedral coordination in **1′** compared to **1** owing to the reduced dimensions of the Ti atom, which can be more easily accommodated in the quasi-planar tetra-oxo matrix.

Frontier orbital analysis performed on complex **1′** revealed a B_1 symmetry LUMO of essentially titanium d_{xz} character, the same spatial orientation found for the LUMO of the Zr analogue **1**; however, the LUMO of **1′** is 0.90 eV higher than that of **1**, suggesting that coordination of the nucleophilic MeNC ligand to the Ti center might be less energetically favored than in the corresponding Zr complex.

We then optimized the structure of the [calix[4](OMe)$_2$(O)$_2$Ti(Me)$_2$]–MeNC adduct, **2a′**, without any symmetry constraints considering only the favored facial

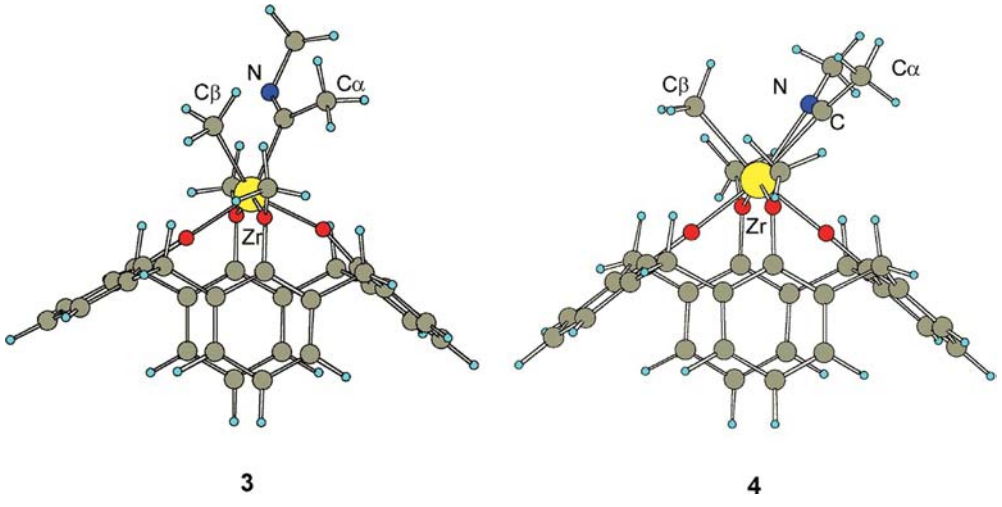

Fig. 8. Optimized structure of the η^1- and η^2-iminoacyl Zr complexes **3** and **4**

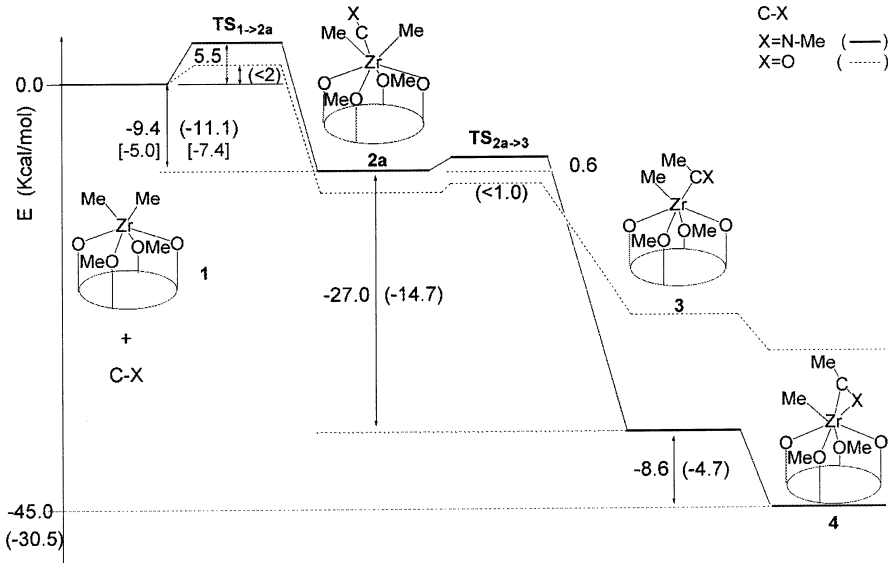

Fig. 9. Computed energetics of MeNC insertion (*solid line*) into the Zr–Me bond compared to the energetics of CO insertion (values in *parentheses*, *dashed line*). The basis set superposition error corrected energetics are reported in *brackets*

coordination. Optimized geometrical parameters are collected in Table 2; again, we found a structure qualitatively similar to that of the zirconium adduct **2a**, with the MeNC group almost lying in the plane bisecting the Me–Ti–Me angle (*xz* plane).

The Ti–CN bond distance is 2.085 Å, i.e. 0.186 Å shorter than in **2a**, in line with the reduction of titanium–carbon bonds already observed for **1′**. Complex **2a′** was found to lie only 0.7 kcal mol^{-1} below the starting reagents (**1′** + MeNC), and 3.7 kcal mol^{-1} above them when accounting for BSSE correction; therefore it is not stable with respect to the free reagents. Such a destabilization of adduct **2a′** with respect to the zirconium analogue **2a** is consistent with the higher value of the LUMO computed for **1′** with respect to **1**, see earlier. Indeed, geometry optimization of the transition state for MeNC coordination led to a structure 12.7 kcal mol^{-1} above the BSSE corrected energy of the free reagents, to be compared to the value of 5.5 kcal mol^{-1} computed for the Zr system, (Fig. 10).

We then optimized the geometry of the transition state for the migratory MeNC insertion leading to the corresponding η^1-iminoacyl, finding a structure only 0.3 kcal mol^{-1} above **2a′**. We therefore see how in this case too the highest energy barrier for the overall MeNC insertion is associated with the coordination step. We finally optimized the structures of the η^1- and η^2-iminoacyl species, **3′** and **4′**, respectively, finding the η^1-iminoacyl **3′** complex to lie 29.8 kcal mol^{-1} below **2a′**, with the η^2-bound isomer still 7.0 kcal mol^{-1} lower in energy. This energy profile is qualitatively similar to that found for the Zr system, showing the η^2-iminoacyl species to be the stable isomer. The main geometrical optimized parameters for **3′** and **4′** are reported in Table 2.

4 Concluding remarks

A summary of the energetics for MeNC coordination and insertion into the Zr–Me bond is reported in Fig. 9, along with the corresponding data obtained for CO

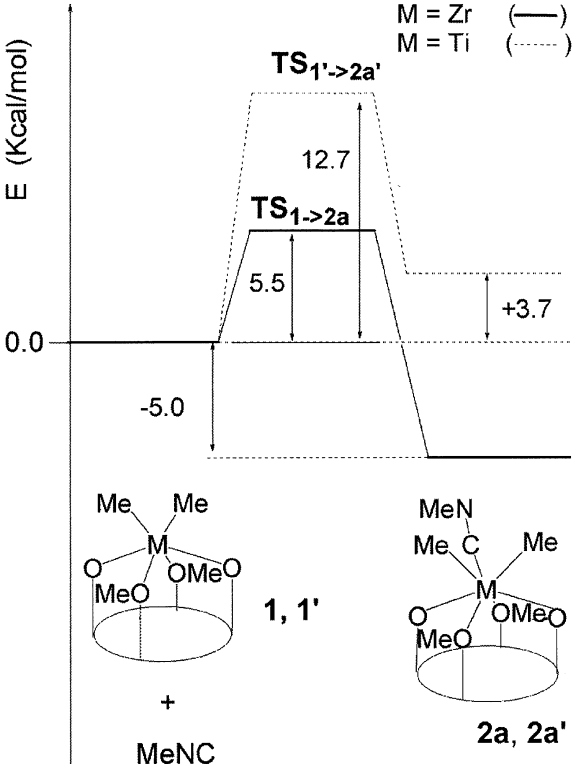

Fig. 10. Comparison of computed energetics for MeNC coordination to the Zr (*solid line*) and Ti (*dashed line*) centres

migration, for direct comparison. Relatively stable facial adducts are found in both cases although a higher barrier to coordination is computed for MeNC (5.5 versus 2.0 kcal mol $^{-1}$). Dynamics simulations have shown that both insertion reactions lead to an η^2-bound acyl (iminoacyl) passing through a labile η^1isomer; however, while in CO insertion the methyl was found to attack the resting carbonyl group, in MeNC insertion the reaction mechanism was found to be reversed, with isocyanide inserting into the Zr–Me bond. Notably, small energy barriers and relatively high exothermicities

are computed both for CO and for MeNC migratory insertions, the slightly higher barrier to MeNC coordination probably being determined by steric factors. It is worth noting that the much higher exothermicity computed for MeNC compared to CO insertion (35.6 versus 19.4 kcal mol^{-1}) is consistent with the broad experimental evidence that isocyanide deinsertion is an extremely rare process at variance with CO deinsertion, where facile deinsertion reactions are customary.

Interestingly, the MeNC coordination to the Ti centre features a higher energy barrier compared to MeNC coordination of the Zr centre (12.7 versus 5.5 kcal mol^{-1}) and leads to a relatively unstable adduct, (Fig. 10), consistent with the frontier orbital analysis performed on the dimethyl–titanium complex **1′**, showing a LUMO 0.90 eV higher in energy than that of the analogue dimethyl–zirconium complex **1**.

References

1. Car R, Parrinello M (1985) Phys Rev Lett 55: 2471
2. Fantacci S, De Angelis F, Sgamellotti A, Re N (2001) Organometallics 20: 4031
3. (a) De Angelis F, Sgamellotti A, Re N (2002) Organometallics 21: 2036; (b) De Angelis F, Sgamellotti A, Re N (2001) J Chem Soc Dalton Trans 1023; (c) De Angelis F, Sgamellotti A, Re N (2000) Organometallics 19: 4104; (d) De Angelis F, Re N, Sgamellotti A, Selloni A, Weber J, Floriani C (1998) Chem Phys Lett 291: 57
4. Kulhmann EJ, Alexander JJ (1980) Coord Chem Rev 33: 195
5. Wojcicki A (1973) Adv Organomet Chem 11: 97
6. Foold TC (1981) In: Geoffry GL (ed) Topics in stereochemistry, vol 12. Wiley, New York, p 83
7. Alexander JJ (1985) In: Hartley FR (ed) The chemistry of the metal–carbon bond, vol 12. Wiley, New York, pp
8. Bock PL, Boschetto DJ, Rasmussen JR, Demeres JP, Whitesides GM (1974) J Am Chem Soc 96: 2814
9. Wax MJ, Bergman RG (1981) J Am Chem Soc 103: 7028
10. (a) Lauher JW, Hoffmann R (1976) J Am Chem Soc 98: 1729; (b) Tatsumi K, Nakamura A, Hofmann P, Stauffert P, Hoffmann R (1985) J Am Chem Soc 107: 4440; (c) Hofmann P, Stauffert P, Tatsumi K, Nakamura A, Hoffmann R (1985) Organometallics 4: 404
11. Durfee LD, Rothwell IP (1988) Chem Rev 88: 1059
12. Chamberlain RL, Durfee LD, Fanwick PE, Kobriger R, Latesky SL, McMullen AK, Rothwell IP, Folting K, Huffman JC, Streib WE, Wang R (1987) J Am Chem Soc 109: 390
13. Chamberlain RL, Durfee LD, Fanwick PE, Kobriger R, Latesky SL, McMullen AK, Steffey BD, Rothwell IP, Folting K, Huffman JC (1987) J Am Chem Soc 109: 6068
14. Giannini L, Caselli A, Solari E, Floriani C, Chiesi-Villa A, Rizzoli C, Re N, Sgamellotti A (1997) J Am Chem Soc 119: 9709
15. Fantacci S, De Angelis F, Sgamellotti A, Re N (2002) Organometallics 21: 4090
16. Fantacci S, Sgamellotti A, Re N, Floriani C (2001) J Chem Soc Dalton Trans 1718
17. Baerends EJ, Ellis DE, Ros P (1973) Chem Phys 2: 42
18. te Velde G, Baerends EJ (1992) J Comput Phys 99: 84
19. Fonseca Guerra C, Visser O, Snijders JG, te Velde G, Baerends EJ (1995) In: Clementi E, Corongiu G (eds) Methods and techniques for comptational chemistry. STEF, Cagliari, p 305
20. http://tc.chem.vu.nl/SCM/Doc/atomicdatabase
21. Vosko SH, Wilk L, Nusair M (1980) Can J Phys 58: 1200
22. Becke AD (1988) Phys Rev A 38: 3098
23. Perdew JP Wang Y (1992) Phys Rev B 45: 13244
24. Powell MJD (1977) Math Prog 12: 241
25. (a) Pasquarello A, Laasonen K, Car R, Lee C, Vanderbilt D (1992) Phys Rev Lett 69: 1982; (b) Pasquarello A, Laasonen K, Car R, Lee C, Vanderbilt D (1993) Phys Rev B 47: 10142
26. Vanderbilt D (1990) Phys Rev B 41: 7892
27. Perdew JP, Zunger A (1981) Phys Rev B 23: 5048
28. Perdew JP, Chevary JA, Vosko SH, Jackson KA, Pederson MR, Singh DJ, Fiolhais C (1992) Phys Rev B 46: 6671
29. (a) Noack K, Calderazzo F (1967) J Organomet Chem 10: 101; (b) Atwood JD (1985) Inorganic and organometallic reaction mechanisms. Brooks/Cole Monterey, CA
30. De Angelis F, Sgamellotti A, Re N (2000) Organometallics 19: 4904